

Complementary Vanadium Dioxide Metamaterial with Enhanced Modulation Amplitude at Terahertz Frequencies

Yuwei Huang,^{1,*} Xuefei Wu,^{1,*} Jacob Schalch,² Guangwu Duan,¹ Chunxu Chen,¹ Xiaoguang Zhao,¹ Kelson Kaj,² Hai-Tian Zhang,³ Roman Engel-Herbert,^{3,4} Richard D. Averitt,^{2,†} and Xin Zhang^{1,‡}

¹*Department of Mechanical Engineering and Division of Materials Science and Engineering,
Boston University, Boston, Massachusetts 02215, USA*

²*Department of Physics, University of California, San Diego, La Jolla, California 92093, USA*

³*Department of Materials Science and Engineering,
the Pennsylvania State University, University Park, Pennsylvania 16802, USA*

⁴*Paul-Drude-Institut für Festkörperelektronik, Leibniz-Institut im
Forschungsverbund Berlin e.V., Hausvogteiplatz 5-7, 10117 Berlin, Germany*

(Dated: June 27, 2022)

One route to create tunable metamaterials is through integration with “on-demand” dynamic quantum materials, such as vanadium dioxide (VO₂). This enables new modalities to create high performance devices for historically challenging applications. Indeed, dynamic materials have often been integrated with metamaterials to imbue artificial structures with some degree of tunability. Conversely, metamaterials can be used to enhance and extend the natural tuning range of dynamic materials. Utilizing a complementary split ring resonator array deposited on a VO₂ film, we demonstrate enhanced terahertz transmission modulation upon traversing the insulator-to-metal transition (IMT) at ~ 340 K. Our complementary metamaterial increases the modulation amplitude of the original VO₂ film from 42% to 68.3% at 0.47 THz upon crossing the IMT, corresponding to an enhancement of 62.4%. Moreover, temperature dependent transmission measurements reveal a redshift of the resonant frequency arising from a giant increase of the permittivity of the VO₂ film. Maxwell-Garnett effective medium theory was employed to explain the permittivity change upon transitioning through the IMT. Our results highlight that symbiotic integration of metamaterial arrays with quantum materials provides a powerful approach to engineer emergent functionality.

I. INTRODUCTION

Metamaterials, and their single layer analogs (metasurfaces), have enabled a plethora of applications and devices by overcoming the limitations of natural materials. This includes subwavelength imaging [1], the realization of a negative refractive index [2], near zero epsilon devices [3], and the demonstration of cloaks and metalenses [4, 5]. Building on these capabilities, active control and tunability in metamaterials could lead to novel modulators, switches, and sensors over a vast span of the electromagnetic spectrum [6–10].

Vanadium dioxide (VO₂) is a tunable quantum material that has been extensively investigated (in large part) because the insulator-to-metal transition (IMT) occurs above room temperature at ~ 340 K [11]. Light, current, and mechanical strain can also drive the IMT, making VO₂ useful for a broad range of applications [8, 12–16]. Upon undergoing the IMT, the optical conductivity changes by four-orders of magnitude over a broad spectral range, making VO₂ a versatile material to integrate with metamaterials to realize nonlinear responses, state switches, and modulators [17, 18]. Recent efforts have focused on combining VO₂ with metamaterials in the terahertz (THz) frequency range to realize switchable broad-

band absorbers, switchable coding and multi-functional devices based on the IMT [19–22].

In order to enhance the THz response and explore the phase transition behavior of VO₂, we deposited a metamaterial array of complementary split ring resonators (SRRs) on a thin film using direct laser writing and photolithography. As described below, the resultant structure exhibits a significantly enhanced THz transmission modulation across the IMT in excess of a pristine VO₂ film. Previous studies of transmission modulation suffer from a high insertion loss ($> 40\%$) [23] or a relatively small amplitude modulation enhancement in comparison to a pristine film [16].

In addition to the functional increase of the THz transmission modulation upon traversing the IMT, the sensitivity of the metamaterial resonators to the surrounding dielectric environment reveals an abnormally large increase of the permittivity of VO₂ during the IMT. This phenomenon can be attributed to insulating and metallic phase coexistence at the onset of the IMT, which has previously been studied by scanning near-field infrared microscopy [24–26]. With increasing temperature, the formation of rutile metallic puddles surrounded by an insulating VO₂ matrix results in an increase in the effective permittivity, as described by Maxwell-Garnett effective medium theory (MG-EMT) [27]. Although Bruggeman EMT has also been employed to explain the IMT [28], our results indicate that MG-EMT better describes the dielectric properties of our integrated metamaterial VO₂ film, especially in the vicinity of the transition [29].

* These two authors contributed equally

† raveritt@ucsd.edu

‡ xinz@bu.edu

In the following, we describe the transmission enhancement properties of integrated metamaterial VO_2 films, highlighting the sensitivity of complementary metamaterial resonators to investigate the mesoscopic phase transition.

II. COMPLEMENTARY VANADIUM DIOXIDE METAMATERIAL

A. Terahertz transmission of pristine vanadium dioxide film

The VO_2 film was deposited on a sapphire substrate by hybrid molecular beam epitaxy using a combinatorial growth [30, 31]. Details of the film growth process can be found in Appendix A. The frequency dependent transmission was measured using THz time domain spectroscopy (THz-TDS) [32]. THz pulses were generated using near infrared (800 nm) pulses generated by a Ti:sapphire laser with a pulse duration of 25 fs. The pulses illuminate a biased photoconductive antenna, and are detected using a similar photoconductive antenna gated by the 800 nm pulses.

THz-TDS transmission measurements of the pristine VO_2 film were performed prior to metamaterial integration. Fig. 1(a) shows the transmission of the VO_2 film at 315 K in the insulating monoclinic phase and at 360 K in the rutile metallic phase ($T_c \sim 340$ K). Near unity transparency is observed close to room temperature for a 100 nm thick VO_2 film in the insulating state (we note that the transmission is referenced to a bare sapphire substrate). Referencing errors caused by birefringent mismatch between the sample and substrate reference along with artifacts arising from an etalon in the sapphire substrates results in small oscillations in the transmission above unity at some frequencies. In the metallic state, the transmission decreases to $\sim 58\%$. This corresponds to a $\sim 42\%$ transmission amplitude modulation between the insulating and metallic states. We note that the flat spectral response in the metallic state arises from the short scattering time of the quasiparticles. The temperature dependent transmission amplitude at 0.47 THz is shown in the inset of Fig. 1. Hysteresis upon heating and cooling is observed as expected for a first order phase transition. Fitting the first derivative of the hysteresis loop to a Gaussian yields a transition temperature with heating of 339 K, and with cooling of ~ 330 K, corresponding to a hysteresis width of 9 K. This dynamic change of transmission under different temperatures makes VO_2 a potential material for tunable THz bandpass filters[33, 34].

B. Design, simulations, and experimental results

Metallic SRR metamaterials exhibit a LC dipole resonance that can modify the transmission modulation of the VO_2 film. For conventional (i.e., not complementary

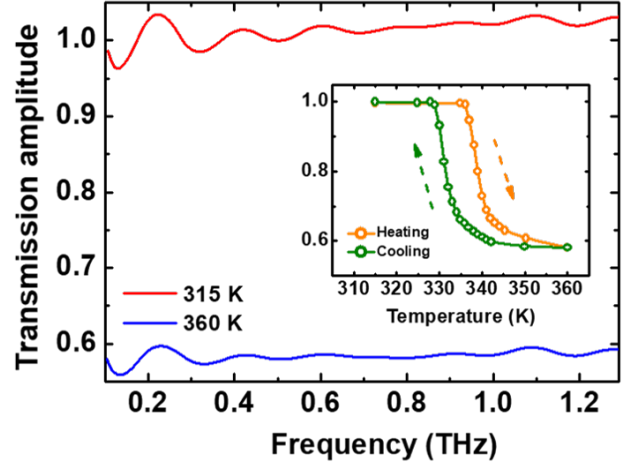


FIG. 1. (a) Terahertz transmission amplitude versus frequency of the pristine VO_2 film in the monoclinic insulating state (red line, 315 K) and rutile metallic phase (blue line, 360 K). Inset is the THz transmission (at 0.47 THz) of the VO_2 film as a function of temperature across the IMT transition. The expected hysteresis is observed upon heating (orange dots – line is guide to eye) and cooling (green dots – line is guide to eye).

– see below) split ring resonators (SRR) on top of a VO_2 film, there is a dip in transmission in the insulating state at the SRR resonance frequency (see Appendix A). Upon traversing the IMT, the transmission will increase since the capacitive gaps of the SRRs are shorted by the metallic VO_2 . In this case, the modulation depth is smaller in comparison to the pristine VO_2 film. However, based on Babinet’s principle [35, 36], a complementary SRR structure exhibits a peak in transmission due to the resonance in the insulating state of VO_2 which can be expected to decrease in the metallic state. Therefore, we investigate the transmission modulation of complementary SRRs integrated with a VO_2 film for enhanced transmission modulation.

An array of complementary split ring resonators (CSRRs) was deposited on a VO_2 film using direct laser writing and photolithography to construct a CSRR- VO_2 metamaterial (CSRR- VO_2 MM). Fig. 2(a) shows an optical image of the array. A 150 nm thick gold film (with a 10 nm Ti adhesion layer) was deposited on the VO_2 film. The lateral dimension of the CSRR is $45 \mu\text{m}$ with a periodicity of $50 \mu\text{m}$, a linewidth of $5 \mu\text{m}$, and slit widths of $3 \mu\text{m}$ on both branches.

The frequency dependent transmission amplitude of the CSRR- VO_2 MM measured using THz-TDS is plotted as dashed lines in Fig. 2(b). The resonance peak occurs at 0.47 THz when the incident light is polarized parallel to the middle gap at 315 K, shown as the blue arrow in Figure 2(a). The transmission amplitude is 82.8% (compared to the pristine VO_2 films, corresponding to an insertion loss of 17.2% – nonetheless the transmission is reasonably high). Conversely, upon fully traversing

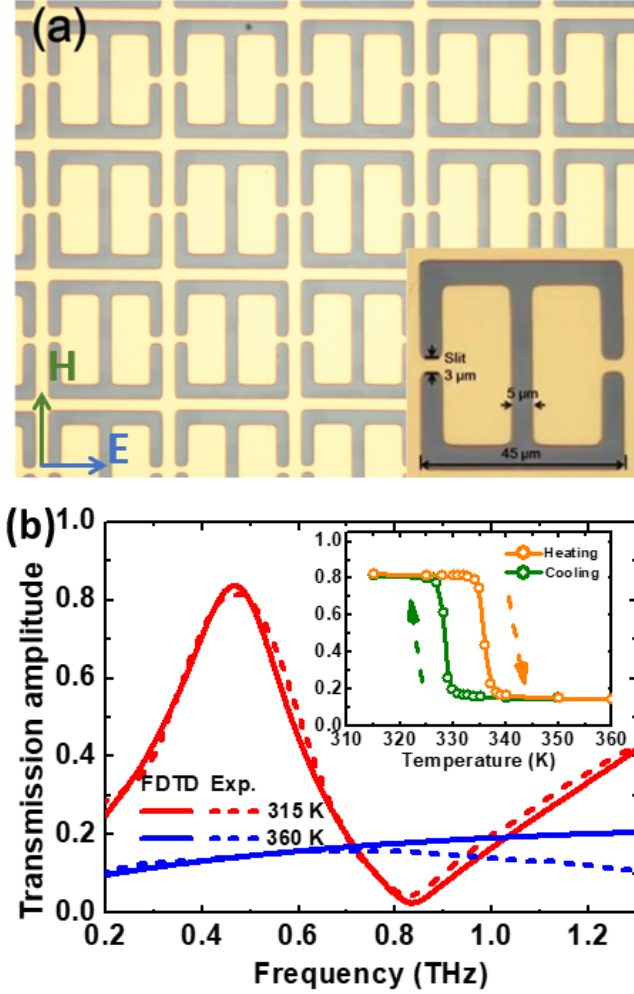


FIG. 2. (a) Microscope image of the CSRR-VO₂ MM on VO₂ film where the inset shows the dimensions of the unit cell. (b) Experimental data (dashed lines) and simulations (solid lines) of the THz transmission of CSRR-VO₂ MM at 315 K (red) and 360 K (blue). Inset is the measurement of temperature-dependent transmission of CSRR-VO₂ MM at 0.47 THz. The solid lines in the inset are a guide to the eye.

to the metallic state to 360 K, no resonant transmission response is evident (blue line, Fig. 2(b)), and the transmission is 14.5% at 0.47 THz. Thus, the modulation amplitude of the THz transmission at 0.47 THz upon crossing the IMT is 68.3%, an increase of 62.4% relative to the bare VO₂ (Fig. 1).

Numerical simulations of the electromagnetic response of the CSRR-VO₂ MM were performed using CST Microwave Studio. The conductivity of gold was taken as 4.5×10^7 S/m. In the insulating state, the VO₂ was modeled using a Drude response with the complex permittivity given by [37, 38] :

$$\epsilon(\omega) = \epsilon_{\infty} - \frac{\omega_p^2}{\omega(\omega + i\gamma)} \quad (1)$$

where the unscreened plasma frequency ω_p is given by

$\sqrt{n_d e^2 / (\epsilon m^*)}$, n_d is the carrier density, e is electron charge, m^* is the carrier effective mass, γ is the scattering frequency ($\gamma = e / \mu m^*$, where μ is the mobility), and $\epsilon_{\infty} = 10$ is the high frequency permittivity. The parameters used in the simulations are shown in Table 1 and the corresponding simulation results are shown as red solid lines in Fig. 2(b). For the metallic state of VO₂, an equivalent carrier density of 10^{21} cm⁻³ at 360 K was used as determined from the THz-TDS measurements of the VO₂ film shown in Fig. 1. The parameters for both the insulating and metallic states in Table 1 are consistent with those in published work [8]. Good agreement with experiment is obtained (Fig. 2(b)) in the metallic state, with a simulated transmission amplitude of 14.7% at 0.47 THz. In addition, the inset in Fig. 2(b) shows the temperature dependence of transmission amplitude at 0.47 THz for the CSRR-VO₂ MM during both heating and cooling. A significant change in the transmission upon heating did not occur until 335 K. Indeed, a dramatic reduction of the transmission occurs within a 2 K span from 335 K to 337 K. Similarly, upon cooling, the transmission recovery occurs at a temperature 5 K lower than the turning point of heating.

The mechanism for the increase in transmission modulation going through the IMT can be partially understood by examining the electric fields and current distributions at the resonant frequencies using full-wave electromagnetic simulations. Fig. 3 shows both the electric field and surface current at the resonant frequency (0.47 THz) when VO₂ is in the insulating state (315 K) and metallic state (360 K). As shown in Fig. 3(a), the electric field in the insulating state is concentrated in the central vertical gap while in the metallic state, this region is electrically shorted, reducing the resonant enhancement of the transmission. The surface currents on the CSRR-VO₂ MM for both states are shown with colored arrows in Fig. 3(c) and (d). The circulating current in Fig. 3(c) is indicative of the lowest energy LC mode of the structure. This is the current path that leads to the enhanced transmission on resonance. However, in the metallic state, the VO₂ film allows current to flow across the central gap, effectively shorting the capacitive region and diminishing the LC mode, as shown in Fig. 2(b), resulting in a low transmission amplitude.

C. Temperature dependence of transmission

Having presented the functional response of the CSRR-VO₂ MM, we now consider the temperature dependence of the transmission upon crossing the IMT in greater detail. Fig. 4(a) and (b) show the experimental transmission spectra at different temperatures during heating and cooling, respectively. Notably, with increased temperature, the resonant frequency dramatically redshifts over a narrow temperature interval, decreasing from 0.47 THz at 334 K to 0.38 THz at 336 K, as shown in Fig. 4(a). A further increase of temperature results in a fully

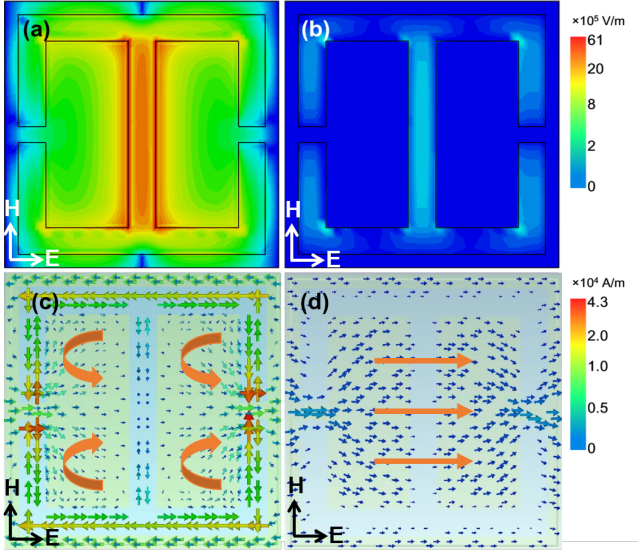


FIG. 3. Simulated electric field of the CSRR-VO₂ MM in the (a) insulating state and (b) metallic state, and the corresponding simulated surface current distributions in the (c) insulating and (d) metallic state at 0.47 THz.

screened resonance, leading to a flat transmission spectrum at 338 K and 360 K. Similar blueshifts can also be observed in Fig. 4(b) during cooling after the resonance peak reappears from 328 K to 315 K.

To clarify the origin of the resonant frequency shifts, we need to consider the frequency dependent dielectric response of the VO₂ film over the temperature range of the IMT. We first consider the Drude response in Eq. (1). Based on the published work, there is a large change of carrier concentration n_d from $\sim 10^{20} \text{ cm}^{-3}$ in the insulating state to $\sim 10^{21} \text{ cm}^{-3}$ in the metallic state, while the mobility μ increases from 1 to 10 $\text{cm}^2/(\text{V}\cdot\text{s})$, and the effective mass m^* decreases from $7 m_0$ to m_0 [39]. Based on the parameters mentioned above, we are able to determine ω_p and γ in both the insulating and the metal state according to Eq. (1).

In order to better understand the redshift of the resonance during IMT, it is useful to express Eq. (1) in terms of the real and imaginary parts of the permittivity:

$$\varepsilon(\omega) = \left(\varepsilon_\infty - \frac{\omega_p^2}{\omega^2 + \gamma^2} \right) + i \frac{\omega_p^2 \gamma}{\omega(\omega^2 + \gamma^2)} = \varepsilon_1 + i\varepsilon_2 \quad (2)$$

We first consider a constant ε_∞ during the IMT. When the temperature increases, n_d increases while m^* decreases, corresponding to an increase of ω_p . Specifically, ω_p increase from $\sim 200 \text{ THz}$ in the insulating state to $\sim 1800 \text{ THz}$ in the metallic state. At the same time, μ increases from 1 to 10, which corresponds to γ decreasing from 250 THz in the insulating state to 170 THz in the metallic state. The combined increase of ω_p and decrease of γ yields a significant decrease of ε_1 at 0.47 THz from 10. We also simulated the response with $\varepsilon_\infty = 10$ while

n , m^* and μ are individually changed (see Appendix C). The simulation results show that the resonant frequency cannot be tuned over 0.1 THz range under constant $\varepsilon_\infty = 10$ even when the transmission amplitude decreases to 0.4. This clearly shows that the Drude response with constant ε_∞ across the IMT cannot account for the experimentally observed frequency shift. Therefore, we must consider additional effects in the VO₂ film during the IMT. Specifically, the experimentally observed redshift indicates that ε_∞ increases in the vicinity of the IMT.

Fig. 4(c) shows the simulation results which includes a significant increase in ε_∞ upon heating, using the parameters in Table 1. Simulations using these values capture the redshift of the resonance observed in experiment. The similar blueshift observed during the cooling process can also be explained by gradually decreasing ε_∞ , as shown in Fig. 4(d) and Table 1.

Given the excellent agreement between simulation and experiment presented in Fig. 4, it is important to understand why the permittivity of VO₂ would exhibit a significant increase during the IMT. In principle, structural changes could lead to huge changes in the permittivity, such as in ferroelectric materials, e.g. BaTiO₃ and CaCu₃Ti₄O₁₂ [40, 41]. On the other hand, scanning near-field infrared microscopy images of polycrystalline VO₂ films indicate a percolative process during the IMT [25, 26, 42]. Metallic puddles emerge, sparsely embedded in the insulating matrix of VO₂, with the volume fraction of the metallic puddles increasing with temperature. At high enough temperatures, the metallic puddles coalesce into a uniform rutile metallic phase (unity metal volume fraction). This process is similar to increasing the concentration of conducting nanoparticles in an otherwise dielectric medium. This can be describe using the Maxwell-Garnett effective medium theory (MG-EMT) model [29]. In this model, the effective permittivity of a dielectric matrix with a metallic volume fraction f of conducting particles is expressed as:

$$\varepsilon_{eff} = \varepsilon_i \frac{\varepsilon_m(1 + 2f) - \varepsilon_i(2f - 2)}{\varepsilon_i(2 + f) + \varepsilon_m(1 - f)} \quad (3)$$

where ε_i is the permittivity in the insulating state, and ε_m is the permittivity in the metallic state. Based on the simulated model, in both the insulating state and metallic state, we used $\varepsilon_i = 10$ and $\varepsilon_m = -90$ between 0.1 to 1.3 THz, in agreement with the published work [24, 43]. Fig. 5(a) shows the relationship between the metallic volume fraction f and the effective permittivity ε_{eff} based on Eq. (3). It is clear that there is a significant increase of the effective permittivity from 10 to ~ 500 when the metallic volume fraction increases to ~ 0.62 along with a sudden decrease and stabilization to -90 when f increases to 1. Combined with the relationship between f and temperature of the VO₂ film during IMT in the published work [44], we are able to estimate the effective permittivity of the VO₂ film at our experimental temperatures (colored stars in Fig. 5(b)). We also include

TABLE I. Permittivity parameters used for the VO₂ simulations.

Process	Temperature (K)	Electron density (cm ⁻³)	Mobility (cm ² /V·s)	Effective mass (m ₀)	ϵ_{∞}
Heating	315	1.0×10^{20}	1.0	7	10
	335	1.2×10^{20}	1.2	6	100
	336	2.3×10^{20}	2.0	5	500
	337	5.0×10^{20}	6.0	3	10
	338	7.0×10^{20}	7.0	2	10
	360	1.0×10^{21}	10.0	1	10
Cooling	330	7.0×10^{20}	7.0	2	10
	329	3.5×10^{20}	5.0	3	200
	328	1.5×10^{20}	1.5	5	250
	327	1.1×10^{20}	1.1	6	50
	315	1.0×10^{20}	1.0	7	10

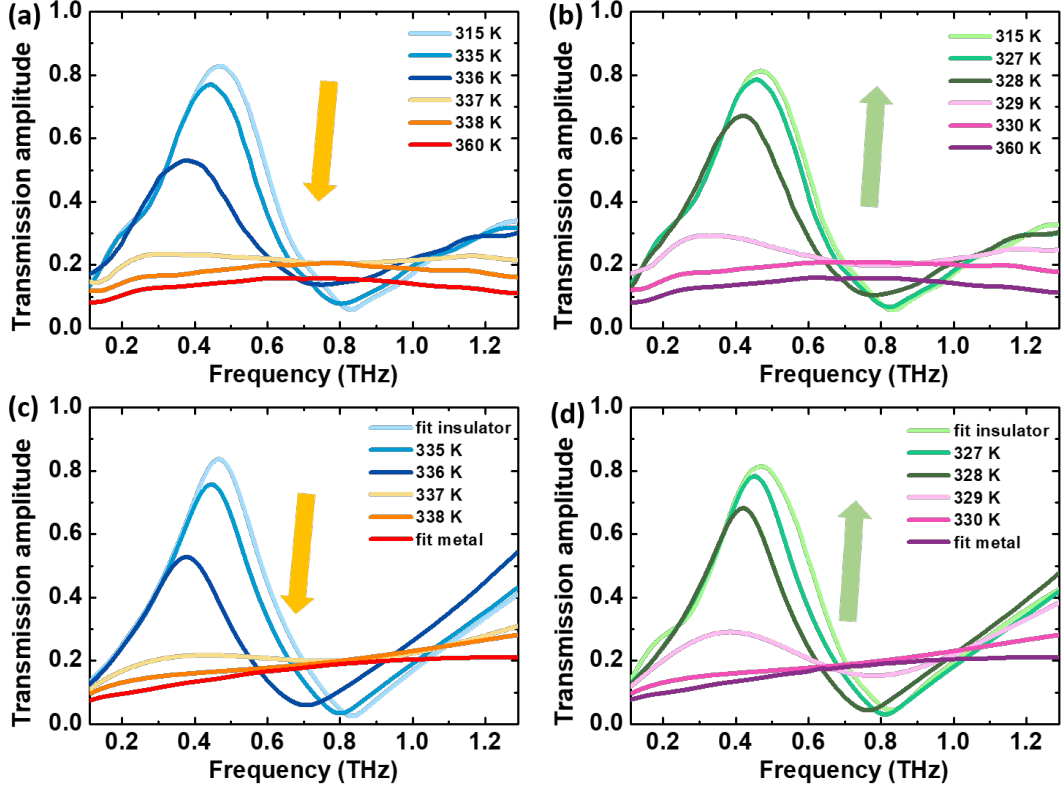


FIG. 4. Experimental and numerical simulation spectra of the VO₂ complementary metamaterial upon crossing the IMT. (a) Experimental heating and (b) cooling results, with corresponding numerical simulations shown in (c) for heating and (d) for cooling using the values from Table 1.

the permittivities used in the simulations at 0.5 THz, shown as the red hollow circles in Fig. 5(b). Reasonable agreement is obtained between the calculated and the simulated permittivity, consistent with a significant permittivity increase during the IMT. We noted that the calculated permittivity at 338 K using Eq. (3) is much lower than the simulated permittivity. This can be attributed to the huge decrease of the calculated permittivity from ~ 400 to ~ -400 when f is between 0.62 to 0.67. Thus, either a slight change of ϵ_m or the f chosen for 338 K would result in a significant change of permittivity at

that temperature. Nonetheless, the trend of the change of permittivity during the IMT used in the simulation is in reasonable agreement with the MG-EMT model. We also calculated the optical conductivities at ~ 0.5 THz (see Appendix D) and the values are also consistent with published work [24].

The Maxwell-Garnett model indicates that the percolation threshold of our VO₂ film is ~ 0.65 . The increases in the metallic volume fraction results in an effective increase in the surface area and narrowing distance between the of the capacitive region of the CSRR. These

combined effects contribute an abnormally large capacitance. A significant permittivity increase occurs in close proximity to the percolation threshold f_t . This is precisely the behavior across the insulator-to-metal transition that results in a giant effective permittivity. This, as our simulations reveal, can account for the observed redshift of the LC resonance. An even higher value of the permittivity of ~ 2700 was achieved with a composite comprised of graphite nanoplates and polyimide, though such a composite lacks the tunability of VO_2 [26].

Above the percolation threshold, the metallic puddles in the VO_2 film coalesce into a uniform metallic film. As such, ϵ_∞ recovers to the original value of 10 and the second term in Eq. (2) dominates, such that the permittivity jumps to an overall negative value [24]. Consequently the metallic VO_2 film shorts the gaps of the CSRR, as shown in Fig. 4(b) and (d).

Our results indicate that, in addition to the enhancement of the transmission modulation across the IMT, integration of the CSRR MM is highly sensitive to the local permittivity. Unlike the very small capacitive gap in a typical SRR, the central “wire” in the complementary structure acts as the capacitive gap, markedly increasing the area of the resonator which probes the local dielectric environment, thereby increasing the overall sensitivity. Furthermore, much of the existing research on VO_2 films focused on effects perpendicular to the plane and thus on the length scale of the film thickness, typically limited to tens to hundreds of nanometers [24]. These scales are too small to observe a significant influence of the percolative effects. In contrast, the relatively large scale of the capacitive region of the CSRR- VO_2 MM structure avoids this limitation. A previous report exhibited this behavior [8], but the complementary structure makes the effect significantly more prominent. That is, the evolution of the CSRR- VO_2 MM resonant frequency across the IMT provides straightforward evidence of the percolative behavior in our VO_2 film.

III. CONCLUSION

We demonstrated metamaterial-enhanced dynamic material properties by integrating a complementary split ring resonator metamaterial directly on a VO_2 film. Relative to the IMT in a pristine VO_2 film, the modulation of the THz transmission (peaked at 0.47 THz) of our hybrid device is enhanced by 62.4%. Moreover, the complementary SRR structure has a larger effective gap area than typical SRR geometries, providing a sensitive probe of the local electrodynamics of the VO_2 . With increasing (decreasing) temperature, we observe a dramatic redshift (blueshift) in the resonant frequency of the CSRR- VO_2 MM structure in a narrow temperature range in the vicinity of the transition temperature. The significant increase of the VO_2 permittivity during the onset of IMT explains the redshift of the resonance. Maxwell-Garnett effective medium theory provides reasonable agreement with ex-

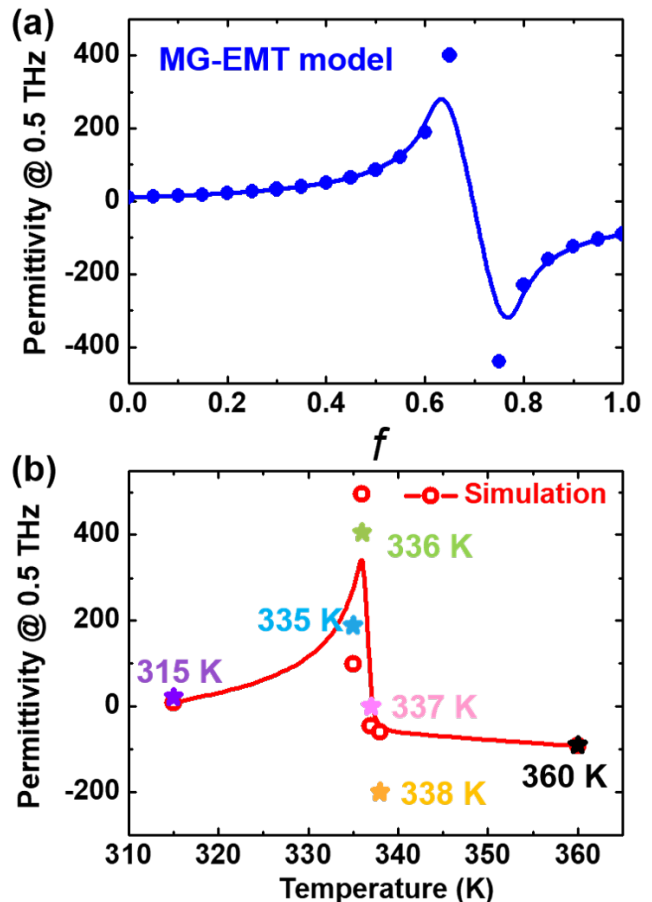


FIG. 5. (a) The metallic volume fraction f dependent permittivity of VO_2 based on Maxwell-Garnett effective medium theory model. (b) Comparison between the permittivity of VO_2 in the simulation (red hollow circles) and the calculation from (a) (colored stars).

periment in describing the temperature dependence of the transmission during IMT. In summary, metamaterials and related metasurface constructs provide a powerful route to obtain dynamic enhancement and dielectric sensitivity that not only facilitates the development of tunable devices, but also provides a simple and effective means to interrogate the local electrodynamic properties of the materials with which they are integrated.

ACKNOWLEDGMENTS

The work at Boston university is supported by National Science Foundation under Grant No. ECCS-1810252. The work at UCSD is supported by ARO MURI Grant No. W911NF-16-1-0361. Film growth (HTZ and REH) was supported by National Science Foundation under Grant No. DMR-1352502 and the Penn State MR-SEC program DMR-1420620.

Appendix A: VO₂ film growth

The VO₂ film was deposited on a sapphire substrate by hybrid molecular beam epitaxy using a combinatorial growth approach. Here, control over the vanadium valence state was achieved by co-supplying elemental vanadium (valence state 0) and the vanadium containing alkoxide precursor vanadium-oxo-triisopropoxide (VTIP), in which vanadium assumes the valence state 5+. Optimal flux ratios were determined using a flux gradient method to establish a valence state library across the wafer during a calibration run. Relative tuning of the two fluxes allowed straight-forward balancing of the vanadium valence state to stabilize the vanadium 4+ state, achieving an epitaxial VO₂ film with excellent uniformity and record-high resistance change across the metal-to-insulator transition exceeding four orders of magnitude [31].

Growth was carried out in DCA M600 MBE growth chamber and VO₂ thin films were grown on a 3-inch r-cut sapphire wafer co-supply of VTIP (vacuum distilled, trace metal impurity 4N, MULTIVALENT Laboratory) using a heated gas inlet system retrofitted to an effusion cell port of the MBE growth chamber and vanadium metal (4N, Ames Laboratory) evaporated from a high temperature Knudsen cell. The respective fluxes were adjusted and maintained via a proportional-integral-derivative (PID)-controlled adjustable leak valve and capacitance manometer on the VTIP gas inlet system and PID controlled Knudsen cell temperature. Sapphire wafer were cleaned in ultrasonic bath of acetone and then isopropanol prior to loading them into the MBE system and baked at 423 K for 2 h in the load lock chamber, subsequently transferred into the MBE growth chamber and heated to the film growth temperature of 623 K. Before deposition substrates were exposed for 20 min to an oxygen plasma (power 250 W, 9×10^{-7} torr oxygen background pressure). The VO₂ film were grown at a rate of about 5 Å min⁻¹ in the presence of an oxygen plasma by co-supplying a vanadium atom flux of 4×10^{12} cm⁻²s⁻¹, calibrated by a quartz crystal monitor prior to growth, and matching the required VTIP flux determined from the experimental valence state library obtained from the valence state library. After growth the VO₂ films were cooled in the presence of oxygen plasma.

Appendix B: SRR & CSRR structure

The LC resonance in a SRR structure manifests as a dip in transmission at 0.47 THz, decreasing the transmission to ~ 0.17 when VO₂ is in insulating state, as shown in Fig. 6(a). In the metallic state, the significant increase in conductivity of the VO₂ film screens the LC resonance in SRR structure, resulting in a featureless transmission spectrum with amplitude of ~ 0.2 . Hence, the modulation amplitude across the IMT in VO₂ is small when using a SRR structure. However, based on Babinet's principle,

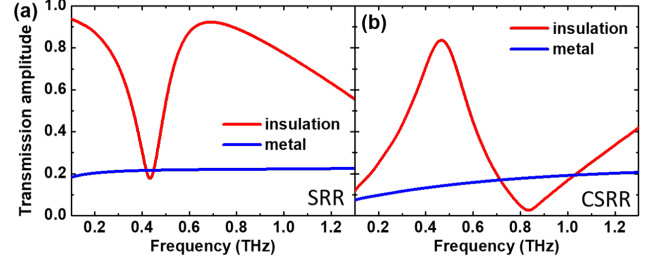


FIG. 6. Simulations of transmission spectra of (a) SRR structure and (b) CSRR structure on VO₂ film in insulating (315 K) and metallic states (360 K).

we are able to achieve transmission peak with amplitude of ~ 0.83 at almost the same frequency using the CSRR structure, as shown in Fig. 6(b). In the insulating state for the CSRR, the transmission is ~ 0.83 decreasing to ~ 0.14 in the metallic state. Therefore, the modulation amplitude is higher using the CSRR structure in comparison to the SRR structure.

Appendix C: Dependence of the resonant frequency on effective mass (m^*), mobility (μ) and carrier density (n)

Based on the Drude model, the dielectric response of VO₂ is determined from the plasma frequency (ω_p) and scattering frequency (γ), which depend on the effective mass (m^*), mobility (μ) and carrier density (n) as described in the manuscript. During the IMT transition, m^* decreases from $7 m_0$ to m_0 , μ increases from 1 to 10 while n_d increases from 10^{20} to 10^{21} cm⁻³. In Fig. 7, we show simulations of the transmission assuming a constant $\epsilon_\infty = 10$. Fig. 7 shows the dependence of the resonant frequency on m^* (Fig. 7(a)), μ (Fig. 7(b)), and n_d (Fig. 7(c)) while holding the other values constant. All three figures show that the resonant frequency exhibits a weak dependence on the three variables, in contrast to the experimental results. Thus, as described in the text and Fig. 4, an increase in ϵ_∞ during the IMT determines the redshift of the resonant frequency.

Appendix D: Conductivity calculated from the imaginary part of permittivity in simulation

Based on the parameters in Table 1, we extract the imaginary part of the permittivity at 0.5 THz from the simulation and calculated the optical conductivity [24]:

$$\sigma_1(\omega) = \frac{\omega \epsilon_2(\omega)}{4\pi} \quad (\text{D1})$$

The results are shown in Fig. 8. The optical conductivity for VO₂ in the metallic state is $\sim 2000 \Omega^{-1}\text{cm}^{-1}$, which is similar to the conductivity in the published work

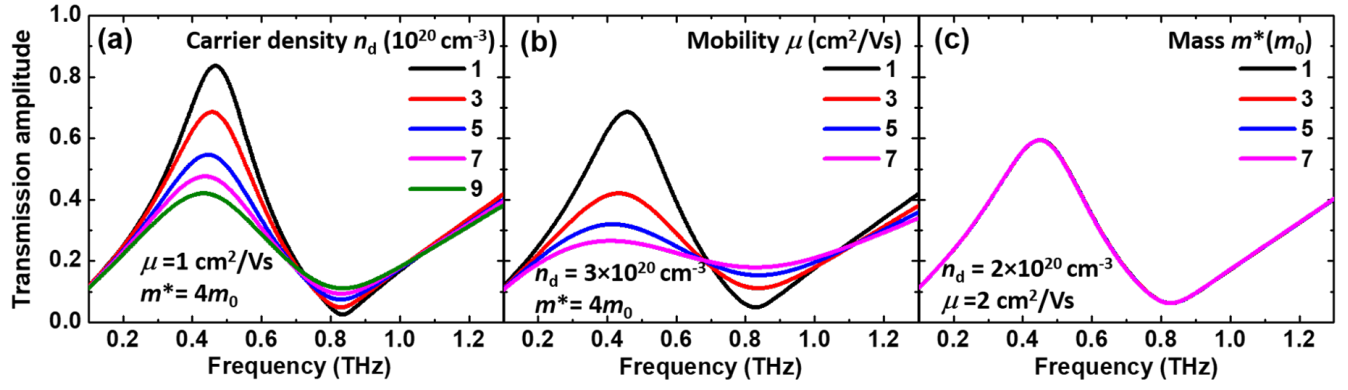


FIG. 7. Dependence of transmission of CSRR-VO₂ MM on (a) effective mass (m^*), (b) mobility (μ) and (c) carrier density (n_d).

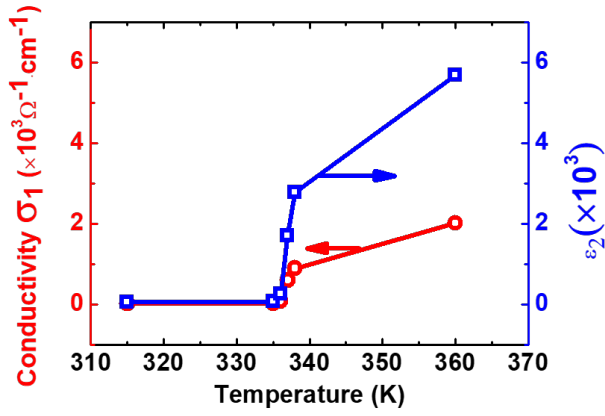


FIG. 8. Imaginary part of permittivity (ϵ_2) extracted from simulations and corresponding real part of conductivity (σ_1) at 0.5 THz.

[24]. The conductivity is closely correlated with polarized metallic particles inside the material.

- [1] C. M. Watts, D. Shrekenhamer, J. Montoya, G. Lipworth, J. Hunt, T. Slesman, S. Krishna, D. R. Smith, and W. J. Padilla, Terahertz compressive imaging with metamaterial spatial light modulators, *Nat. Photonics* **8**, 605 (2014).
- [2] D. R. Smith, J. B. Pendry, and M. C. Wiltshire, Metamaterials and negative refractive index, *Science* **305**, 788 (2004).
- [3] R. Maas, J. Parsons, N. Engheta, and A. Polman, Experimental realization of an epsilon-near-zero metamaterial at visible wavelengths, *Nat. Photonics* **7**, 907 (2013).
- [4] X. Ni, Z. J. Wong, M. Mrejen, Y. Wang, and X. Zhang, An ultrathin invisibility skin cloak for visible light, *Science* **349**, 1310 (2015).
- [5] M. Khorasaninejad and F. Capasso, Metalenses: Versatile multifunctional photonic components, *Science* **358** (2017).
- [6] H.-T. Chen, W. J. Padilla, J. M. Zide, A. C. Gossard, A. J. Taylor, and R. D. Averitt, Active terahertz metamaterial devices, *Nature* **444**, 597 (2006).
- [7] X. Zhao, J. Schallch, J. Zhang, H. R. Seren, G. Duan, R. D. Averitt, and X. Zhang, Electromechanically tunable metasurface transmission waveplate at terahertz frequencies, *Optica* **5**, 303 (2018).
- [8] M. Liu, H. Y. Hwang, H. Tao, A. C. Strikwerda, K. Fan, G. R. Keiser, A. J. Sternbach, K. G. West, S. Kittiwatanakul, J. Lu, *et al.*, Terahertz-field-induced insulator-to-metal transition in vanadium dioxide metamaterial, *Nature* **487**, 345 (2012).
- [9] K. Fan, H. Y. Hwang, M. Liu, A. C. Strikwerda, A. Sternbach, J. Zhang, X. Zhao, X. Zhang, K. A. Nelson, and R. D. Averitt, Nonlinear terahertz metamaterials via field-enhanced carrier dynamics in gaas, *Phys. Rev. Lett.* **110**, 217404 (2013).
- [10] Y. Huang, K. Kaj, C. Chen, Z. Yang, S. R. Ul Haque, Y. Zhang, X. Zhao, R. D. Averitt, and X. Zhang, Broadband terahertz silicon membrane metasurface absorber, *ACS Photonics* **9**, 1150 (2022).
- [11] F. Morin, Oxides which show a metal-to-insulator transition at the neel temperature, *Phys. Rev. Lett.* **3**, 34 (1959).
- [12] J. Cao, E. Ertekin, V. Srinivasan, W. Fan, S. Huang, H. Zheng, J. Yim, D. Khanal, D. Ogletree, J. Grossman, *et al.*, Strain engineering and one-dimensional organization of metal-insulator domains in single-crystal vanadium dioxide beams, *Nat. Nanotechnol.* **4**, 732 (2009).
- [13] B. T. O'callahan, A. C. Jones, J. H. Park, D. H. Cobden, J. M. Atkin, and M. B. Raschke, Inhomogeneity of the ultrafast insulator-to-metal transition dynamics of vo2, *Nat. Commun.* **6**, 1 (2015).
- [14] J. Jeong, N. Aetukuri, T. Graf, T. D. Schladt, M. G. Samant, and S. S. Parkin, Suppression of metal-insulator transition in vo2 by electric field-induced oxygen vacancy formation, *Science* **339**, 1402 (2013).
- [15] Z. Tao, T.-R. T. Han, S. D. Mahanti, P. M. Duxbury, F. Yuan, C.-Y. Ruan, K. Wang, and J. Wu, Decoupling of structural and electronic phase transitions in vo2, *Phys. Rev. Lett.* **109**, 166406 (2012).
- [16] H. Zhu, J. Li, L. Du, L. Shan, P. Li, X. Lu, T. Feng, S. Das, W. Huang, Q. Shi, *et al.*, Vo2-metallic hybrid metasurfaces for agile terahertz wave modulation by phase transition, *APL Materials* **10**, 031112 (2022).
- [17] L. Liu, L. Kang, T. S. Mayer, and D. H. Werner, Hybrid metamaterials for electrically triggered multifunctional control, *Nat. Commun.* **7**, 1 (2016).
- [18] S. Cuffe, D. Li, Y. Zhou, F. J. Wong, J. A. Kurvits, S. Ramanathan, and R. Zia, Dynamic control of light emission faster than the lifetime limit using vo2 phase-change, *Nat. Commun.* **6**, 1 (2015).
- [19] J. Li, Y. Zhang, J. Li, J. Li, Y. Yang, J. Huang, C. Ma, Z. Ma, Z. Zhang, L. Liang, *et al.*, Frequency-switchable vo2-based coding metasurfaces at the terahertz band, *Optics Commun.* **458**, 124744 (2020).
- [20] J.-S. Li and X.-J. Li, One-dimensional terahertz dielectric gradient metasurface for broadband spoof surface plasmon polaritons couplers, *Opt. Express* **30**, 12823 (2022).
- [21] J. Shabanpour, S. Beyraghi, and A. Cheldavi, Ultrafast reprogrammable multifunctional vanadium-dioxide-assisted metasurface for dynamic thz wavefront engineering, *Sci. Rep.* **10**, 1 (2020).
- [22] F. Ding, S. Zhong, and S. I. Bozhevolnyi, Vanadium dioxide integrated metasurfaces with switchable functionalities at terahertz frequencies, *Adv. Opt. Mater.* **6**, 1701204 (2018).
- [23] M. Seo, J. Kyoung, H. Park, S. Koo, H.-s. Kim, H. Bernien, B. J. Kim, J. H. Choe, Y. H. Ahn, H.-T. Kim, *et al.*, Active terahertz nanoantennas based on vo2 phase transition, *Nano Lett.* **10**, 2064 (2010).
- [24] M. M. Qazilbash, M. Brehm, B.-G. Chae, P.-C. Ho, G. O. Andreev, B.-J. Kim, S. J. Yun, A. Balatsky, M. Maple, F. Keilmann, *et al.*, Mott transition in vo2 revealed by infrared spectroscopy and nano-imaging, *Science* **318**, 1750 (2007).
- [25] M. Qazilbash, M. Brehm, G. Andreev, A. Frenzel, P.-C. Ho, B.-G. Chae, B.-J. Kim, S. J. Yun, H.-T. Kim, A. Balatsky, *et al.*, Infrared spectroscopy and nano-imaging of the insulator-to-metal transition in vanadium dioxide, *Phys. Rev. B* **79**, 075107 (2009).
- [26] F. He, S. Lau, H. L. Chan, and J. Fan, High dielectric permittivity and low percolation threshold in nanocomposites based on poly (vinylidene fluoride) and exfoliated graphite nanoplates, *Adv. Mater.* **21**, 710 (2009).
- [27] J. M. Garnett, Vii. colours in metal glasses, in metallic films, and in metallic solutions.—ii, *Philosophical Transactions of the Royal Society of London. Series A, Containing Papers of a Mathematical or Physical Character* **205**, 237 (1906).
- [28] H. Liu, Z.-H. Wang, L. Li, Y.-X. Fan, and Z.-Y. Tao, Vanadium dioxide-assisted broadband tunable terahertz metamaterial absorber, *Sci. Rep.* **9**, 1 (2019).
- [29] P. U. Jepsen, B. M. Fischer, A. Thoman, H. Helm, J. Suh, R. Lopez, and R. Haglund Jr, Metal-insulator phase transition in a vo2 thin film observed with terahertz spectroscopy, *Phys. Rev. B* **74**, 205103 (2006).
- [30] M. Brahlek, A. S. Gupta, J. Lapano, J. Roth, H.-T. Zhang, L. Zhang, R. Haislmaier, and R. Engel-Herbert, Frontiers in the growth of complex oxide thin films: past, present, and future of hybrid mbe, *Adv. Funct. Mater.* **28**, 1702772 (2018).
- [31] H.-T. Zhang, L. Zhang, D. Mukherjee, Y.-X. Zheng, R. C. Haislmaier, N. Alem, and R. Engel-Herbert, Wafer-scale growth of vo2 thin films using a combinatorial approach,

- Nat. Commun. **6**, 1 (2015).
- [32] X. Zhao, J. Schalch, J. Zhang, H. R. Seren, G. Duan, R. D. Averitt, and X. Zhang, Electromechanically tunable metasurface transmission waveplate at terahertz frequencies, *Optica* **5**, 303 (2018).
 - [33] Y. Huang, Q. He, D. Zhang, and Y. Kanamori, Switchable band-pass filter for terahertz waves using vo2-based metamaterial integrated with silicon substrate, *Opt. Rev.* **28**, 92 (2021).
 - [34] T. Li, X. Luo, F. Hu, G. Li, W. Xu, Y. Zhou, Z. Wang, X. Zhang, L. Zhang, and Y. Wang, Terahertz bandstop-to-bandpass converter based on vo2 hybrid metasurface, *J. Phys. D: Appl. Phys.* **54**, 435105 (2021).
 - [35] T. Zentgraf, T. Meyrath, A. Seidel, S. Kaiser, H. Giessen, C. Rockstuhl, and F. Lederer, Babinet's principle for optical frequency metamaterials and nanoantennas, *Phys. Rev. B* **76**, 033407 (2007).
 - [36] X. Zhao, C. Chen, K. Kaj, I. Hammock, Y. Huang, R. D. Averitt, and X. Zhang, Terahertz investigation of bound states in the continuum of metallic metasurfaces, *Optica* **7**, 1548 (2020).
 - [37] T. Cocker, L. Titova, S. Fourmaux, H.-C. Bandulet, D. Brassard, J.-C. Kieffer, M. El Khakani, and F. Hegmann, Phase diagram of the ultrafast photoinduced insulator-metal transition in vanadium dioxide, *Appl. Phys. Lett.* **97**, 221905 (2010).
 - [38] C. Berglund and H. Guggenheim, Electronic properties of v o 2 near the semiconductor-metal transition, *Phys. Rev.* **185**, 1022 (1969).
 - [39] J. H. Park, J. M. Coy, T. S. Kasirga, C. Huang, Z. Fei, S. Hunter, and D. H. Cobden, Measurement of a solid-state triple point at the metal-insulator transition in vo2, *Nature* **500**, 431 (2013).
 - [40] A. Litvinchuk, C. Chen, N. Kolev, V. Popov, V. Hadjiev, M. Iliev, R. Bontchev, and A. Jacobson, Optical properties of high-dielectric-constant cacu3ti4o12 films, *Phys. Status Solidi A* **195**, 453 (2003).
 - [41] Z.-M. Dang, J.-K. Yuan, S.-H. Yao, and R.-J. Liao, Flexible nanodielectric materials with high permittivity for power energy storage, *Adv. Mater.* **25**, 6334 (2013).
 - [42] M. Liu, M. Wagner, E. Abreu, S. Kittiwatanakul, A. McLeod, Z. Fei, M. Goldflam, S. Dai, M. Fogler, J. Lu, *et al.*, Symmetry breaking and geometric confinement in vo2: Results from a three-dimensional infrared nano-imaging, *Phys. Rev. Lett.* **111**, 096602 (2013).
 - [43] N. Émond, B. Torriass, D. Morris, and M. Chaker, Natural metamaterial behavior across the phase transition for wxv1- xo2 films revealed by terahertz spectroscopy, *Acta Mater.* **140**, 20 (2017).
 - [44] D. Hilton, R. Prasankumar, S. Fourmaux, A. Cavalleri, D. Brassard, M. El Khakani, J. Kieffer, A. Taylor, and R. Averitt, Enhanced photosusceptibility near t c for the light-induced insulator-to-metal phase transition in vanadium dioxide, *Phys. Rev. Lett.* **99**, 226401 (2007).
 - [45] C.-W. Nan, Y. Shen, and J. Ma, Physical properties of composites near percolation, *Annu. Rev. Mater. Sci.* **40**, 131 (2010).